Technical Paper
J. Astron. Space Sci. 41(2), 121-138 (2024)
https://doi.org/10.5140/JASS.2024.41.2.121

JASS Journal of Astronomy and Space Sciences

Short Wave Infrared Imaging for Auroral Physics and Aeronomy Studies

Trond S. Trondsen[1†], John Meriwether[2], Craig Unick[1], Andrew Gerrard[2], Matthew Cooper[2], Devin Wyatt[1]

[1]Keo Scientific Ltd., Calgary, AB T2Z 4M3, Canada
[2]Center for Solar-Terrestrial Research, New Jersey Institute of Technology, Newark, NJ 07102-1982, USA

Advances in solar-terrestrial physics are generally linked to the development of innovative new sensor technologies, affording us ever better sensitivity, higher resolution, and broader spectral response. Recent advances in low-noise InGaAs sensor technology have enabled the realization of low-light-level scientific imaging within the short-wave infrared (SWIR) region of the electromagnetic spectrum. This paper describes a new and highly sensitive ultra-wide angle imager that offers an expansion of auroral and airglow imaging capabilities into the SWIR spectral range of 900–1,700 nm. The imager has already proven successful in large-area remote sensing of mesospheric temperatures and in providing intensity maps showing the propagation and dissipation of atmospheric gravity waves and ripples. The addition of an automated filter wheel expands the range of applications of an already versatile SWIR detector. Several potential applications are proposed herein, with an emphasis on auroral science. The combined data from this type of instrument and other existing instrumentation holds a strong potential to further enhance our understanding of the geospace environment.

Keywords: auroral imaging, aurora, airglow, all-sky imager, short-wave infrared (SWIR), InGaAs sensors

1. INTRODUCTION

Transformational leaps forward in scientific discovery are often associated with advances in technology and instrumentation. This holds particularly true when it comes to the application of all-sky imagers to the mesoscale mapping of spatial brightness distributions of aurora and airglow. Previous imaging research efforts, as summarized in the reviews of Eather (1967, 1975, 1988), Bosqued (1985), Baumgardner et al. (1993, 2007), Galand (2001), Galand & Chakrabarti (2006), Frey (2007), Martinis et al. (2018), and others, demonstrate that imaging has been extremely useful as a tool for ground-based remote sensing of the geospace environment. The first imagers fielded in the 1960s and earlier were film-based. Eventually, these were replaced by imagers using image intensifier tubes (later versions incorporating GaAs photocathodes on microchannel plates) and then Si (silicon) detectors, such as the charge-coupled device (CCD). The increased sensitivity led to higher cadence while achieving excellent imaging of weak spectral emissions, such as the H_β emission. Thus, impactful auroral and airglow studies observing a wide range of atomic and molecular emissions within the visible to near-infrared range of 400–900 nm emerged.

The recent development of larger-area, deep-cooled InGaAs (indium gallium arsenide) focal-plane arrays presents a unique opportunity to expand geospace imaging science into the previously under-explored short-wave infrared (SWIR) spectral range of 900–1,700 nm. Keo Scientific Ltd. has recently developed and commercialized a state-of-the-art, compact SWIR imager, the Keo *Sentry-SWIR*, with the aim of engendering new aeronomy and auroral physics studies by exploration of the imaging of auroral and airglow emissions within the SWIR wavelength range. The instrument

Received 06 MAR 2024 **Revised** 20 APR 2024 **Accepted** 10 MAY 2024
†**Corresponding Author**
Tel: +1-403-452-7222, E-mail: trondsen@keoscientific.com
ORCID: https://orcid.org/0000-0002-9538-1832

is described in more detail in Section 2.

The instrument has already been successfully deployed and utilized in the more specific application developed by Pautet et al. (2014). This is a technique designed to study mesosphere dynamics by measuring precise high-cadence maps of OH rotational temperatures and intensities using two selected OH emissions from the 3-1 OH P branch in the SWIR region near 1,500 nm. This wavelength range benefits from a lack of auroral contamination in the spectral regions sampled for polar observations, as well as by the much stronger OH intensities accessible in the SWIR region as compared with the OH emissions within the visible region of the spectrum commonly used in the past to observe OH rotational temperature (Meriwether 1975; Taylor et al. 2001). This paper briefly discusses the application of the Keo *Sentry-SWIR* to this technique while also proposing several other applications that warrant further investigation, *viz.*:

- Studying the spatial morphology of the high latitude and cusp energetic particle deposition distributions with respect to helium (He) aurora, proton auroras, and electron auroras for quiet and active geomagnetic periods.
- Searching for possible sub-auroral manifestations of energetic He, hydrogen (H), and electron phenomena associated with features known as "spot" aurora, detached sub-auroral forms, STEVE, SAR arcs, and proton flashes (e.g., Frey 2007; Gallardo-Lacourt et al. 2021).
- Identifying the auroral morphology relating to Alfvénic auroras, i.e., auroras that have been created by electron acceleration through fast-moving Alfvén waves generated within the magnetosphere by geomagnetic field line oscillations. This approach would be based upon measurements of the N_2^+ Meinel rotational temperature obtained by measuring the "head" and "tail" brightnesses of the 0-0 Meinel band with origin at 1,105.0 nm. Comparing this temperature with the Mass-Spectrometer-Incoherent-Scatter (MSIS) model temperature profile would allow the determination of the altitude of the source auroral emission, and thus inferring the characteristic energy of electron precipitation creating the auroral emission, as pioneered by Hunten et al. (1963).
- Determining the typical behavior of the He nightglow with respect to seasonal, nocturnal, and short-term 1,083 nm intensity variations. This would represent a new, novel approach to the study of He density variability and its sensitivity to changes in the total atmospheric density and global circulation dynamics across an extensive latitude range of ~12°.

Many other applications can be envisioned, but these ideas illustrate the possible scope of the applications that imaging the SWIR spectral emissions might provide.

In summary, the extension of geospace imaging science into the SWIR region of the electromagnetic spectrum has the potential to broaden the range of space weather explorations, with a promise of facilitating additional advancements in our understanding of the geospace environment as observed from the ground. Also, SWIR imaging might well enable improved diagnostic measurements in support of currently existing instrumentation and facilities (Beedle et al. 2022).

2. INSTRUMENTATION

2.1 Instrumental Details

The Keo *Sentry-SWIR* imager, with a cross-section diagram, is pictured in Fig. 1. The design of the imager is based on Keo Scientific's traditional CCD all-sky imager, successfully employed for visible-range imaging by research groups world-wide since the early 1990s.

As there are no commercially available SWIR fisheye lenses with the characteristics required for the detection of

Fig. 1. The Keo *Sentry-SWIR* ultra-wide angle imager. The bottom panel shows a cross-section schematic of the instrument. SWIR, short-wave infrared.

low-light-level airglow and aurora emissions, the imager's fisheye lens was custom-designed and manufactured by Keo Scientific specifically for this instrument (Trondsen et al. 2021). This primary lens is a 30 mm focal length, f/3.5 fisheye (180°) optimized and anti-reflection (AR) coated for the wavelength range of 1,000–1,700 nm.

The circular field of view (FoV) of the instrument is set to 120° at the primary image plane by means of a Lyot stop. The reason for limiting the field of view to 120° in this application is that, for a given sensor size and pixel pitch, there is always a tradeoff between spatial coverage and spatial resolution. This is particularly true for InGaAs sensors, which remain relatively small and have a limited number of pixels compared to CCD sensors. Data from the Advanced infrared Mesospheric Temperature Mapper (AMTM) of Pautet et al. (2014) have already shown 120° to be an acceptable compromise given the spatial scales of phenomena of interest, such a mesospheric gravity waves (GWs) and ripples. Additionally, the aperture of the primary lens is stopped down to f/5, which achieves the intended f/1 imaging at the sensor through preservation of the Lagrange Invariant (etendue).

The Lyot stop, in conjunction with specially applied internal paints, also plays a critical role in minimizing scattered light within the imager. The fisheye lens is followed by a capping shutter, closed during daytime to protect filters and sensor from direct exposure to the sun.

The optical design is image-space telecentric, ensuring that the principal ray of all image-forming cones across the field of view intersects the image plane parallel to the optical axis (Baumgardner et al. 1993). This characteristic allows for the utilization of interference filters as narrow as 1.0 nm FWHM, with the maximum ray angle through the filter depending only on the f-number of the fisheye lens. The cone angle of the AMTM of Pautet et al. (2014), is approximately f/11 whereas the cone angle of the Keo *Sentry-SWIR* is f/5, resulting in a significantly more compact instrument size. Interference filters are essentially etalons and ray-angles and thermal environment must therefore be carefully controlled. The filter wheel is thermally stabilized to ± 0.1°C and accepts up to eight 3-inch diameter filters. In SWIR imaging systems, signal contribution from thermal photons emitted by internal imager components (such as the shutter that is closed during dark-frame acquisition) cannot be ignored. To address this, Keo Scientific devised a custom filter with zero transmission, yet possessing the same effective emissivity as the filters used during sky imaging. This filter is rotated into the optical path during the acquisition of images later used for dark-frame subtraction.

Next, the large primary image at the filter plane is reimaged at a fast speed of f/1.0 onto a state-of-the-art, 640 × 512 pixels (12.8 mm × 10.24 mm, 20 μm pixel pitch) InGaAs focal-plane array. InGaAs sensors, which have a hybrid structure consisting of back-illuminated InGaAs photodiodes and a complementary metal-oxide semiconductor (CMOS) readout circuit, are noisy compared to CCDs, but have an acceptable dark current performance when deep-cooled. The Keo *Sentry-SWIR* leverages a Teledyne Princeton Instruments NIRvana 640, which is thermoelectrically cooled to –80°C.

An absolute calibration of the imager is performed by Keo Scientific personnel to establish a relationship between arbitrary, instrument-dependent raw pixel values (counts) and photon flux (apparent emission rate) in physical units of rayleighs (R). Absolute calibration of the imager is a multi-stage process: First, filter bandpass curves are established by using a tunable SWIR laser. Then, on-axis broadband sensitivity is established for each filter by imaging the output of a calibrated, NIST-traceable integrating sphere through the imager, including the filter, and onto the InGaAs sensor. Additionally, an on-axis 'at-wavelength' sensitivity is measured for each filter using a collimated laser beam calibrated with a NIST-traceable optical power meter through the imager, including the filter, and onto the InGaAs array. This all results in the final Absolute Calibration Coefficients, valid on-axis. Finally, a flat-field correction procedure is performed to compensate for off-axis vignetting, resulting in Uniformity Coefficients, one for each filter, allowing one to apply on-axis Absolute Calibration Coefficients to any pixel in the image.

3. CANDIDATE SWIR EMISSIONS FOR AURORA/AIRGLOW STUDIES

3.1 SWIR Emissions Overview

The successful application of any SWIR imager to specific problems hinges on a thorough understanding of the wavelengths and anticipated brightness levels of potential emissions. Saum & Benesch (1970a, b) published SWIR laboratory spectra for N and O and molecular band systems of N_2^+ (Meinel) and N_2 1PG. Examples of SWIR auroral spectra were obtained by Vallance Jones & Gattinger (1976) and Gattinger & Vallance Jones (1981). High-resolution SWIR spectra were published by Baker et al. (1977) and by Baker et al. (1985), providing wavelengths of auroral emissions and their surface brightness. Also useful are the SWIR astronomical high-resolution nightglow spectra published by Rousselot et al. (2000). Baker et al. (1977)

investigated the potential impact of water vapor absorption and concluded that it posed no significant concerns for the SWIR region.

Figs. 2 and 3 exhibit auroral and airglow spectra seen in the SWIR region for the spectral range of 880–1,650 nm (Baker et al. 1985). These spectra exhibit a variety of interesting atomic and molecular emissions. Table 1 presents some selected auroral and airglow emissions that may be of particular interest in SWIR imaging applications. The two Paschen H lines have not yet been identified in auroral or nightglow spectra. However, existing SWIR auroral spectra have all been collected in bright IBC III electron aurora, a scenario where the likelihood of detecting these hydrogen emissions would be low. Special attention is required when measuring the metastable He 1,083 nm multiplet, and this is the topic of the next section.

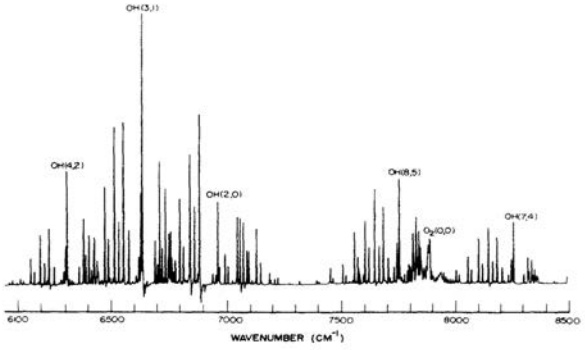

Fig. 2. A ground-based nightglow spectrum obtained at Andøya, Norway on 16 November 1980 using a SWIR Michaelson Connes wide-field interferometer and a Germanium detector. The molecular emission of O_2 (1Δ) and rotational lines of OH band emissions are identified. SWIR, short-wave infrared.

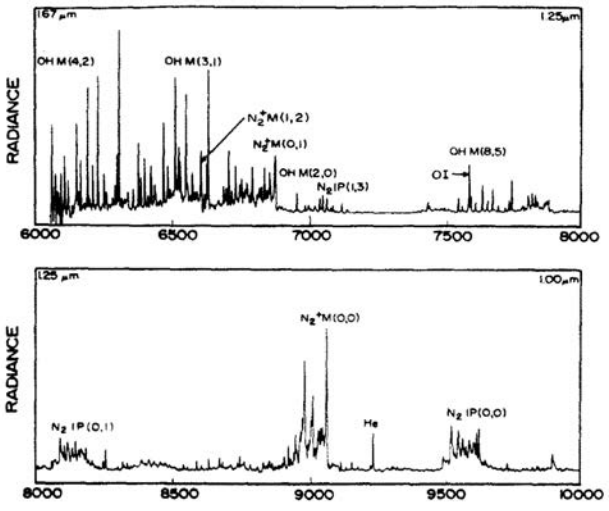

Fig. 3. Auroral SWIR spectra obtained at Andøya on 11 November 11, 1980. Upper panel, from 1,650 nm to 1,250 nm and lower panel, from 1,250 nm to 1,000 nm. The molecular emissions of OH and N_2^+ are identified. SWIR, short-wave infrared.

3.2 The Spectral Structure and Analysis of the Metastable He 1,083 nm Emission

The accurate measurement of the He 1,083 nm multiplet intensity is challenging. Fig. 4 illustrates the spectral structure of the three He 1,083 nm multiplet lines and the four Q branch OH emissions from the 5–2 band that are all located within a narrow range of 0.2 nm near 1,083 nm (Shefov et al. 2009). This example shows the He multiplet intensity as being comparable to the OH Q branch intensities (~1 kR). However, Shefov & Semenov (2011) cited several references indicating that a more typical brightness for the metastable He 1,083 nm multiplet aurora is ~10 kR.

To effectively isolate the spectral features situated within this narrow (0.2 nm) region, high resolution spectrographic or interferometric techniques are usually required. This is because all these features manifest simultaneously within the ~1.0 nm minimum practically feasible filter bandwidth of a telecentric imager so that the intensities for the He 1,083 nm emission and the two Q_1 and Q_2 OH emissions are not separated but blended together. However, we suggest that estimating the metastable He 1,083 nm multiplet intensity by means of an imager is possible by using a novel analysis procedure that is based upon using the intensity data for the $P_1(3)$ images (1,097.5 nm) to compute Q_1 and Q_2 images at 1,083 nm that can be used to correct the observed He 1,083 image.

One approach to achieving this is to compute the Q branch OH intensity contributions to the composite (helium plus the Q_1 and Q_2 Q-components) 1,083 nm image through the application of a rotational temperature. Knowledge of the OH 5-2 band profile from a synthetic spectra model combined with precise measurements of the rotational temperature or using a value taken from the MSIS-00 model would enable the Q_1 and Q_2 branch brightnesses to be estimated based on the observed $P_1(3)$ brightness. This approach is based upon the application of a P/Q branching ratio to yield the Q_1 and Q_2 images that can both be applied to the composite 1,083 nm image for the purpose of removing the OH contamination, leaving only the He contribution.

First, the data for both He 1,083 and the OH 1,097.5 filters would be treated to subtract the continuum background measured at 1,080 nm. In this step, we account for the subtle variations in the transmission profiles of the three filters, which are practically identical with peak transmissions of ~92%–93% (private communication, Alluxa, Inc.). These two

Table 1. Selected auroral and airglow atomic and molecular emissions that might be of interest in SWIR imaging applications

Emission ID	Species	Wavelength [nm]-air	Contamination	Notes
He ($3S\ ^3P$-^3S)	He	1,083.0	3 lines multiplet, contamination from four OH Q branch components	Charge exchange of He^{++}, He^+; excitation by photo-electrons and energetic electrons; Shefov et al. (2009) indicated typical aurora He brightness of ~10 kR
P_β (3-5)	H	1,281.81	Not seen in Vallance Jones & Gattinger (1976) or Baker et al. (1985) auroral spectra, but likely in proton aurora	Charge exchange of H^+; typical brightness unknown
P_γ (3-6)	H	1,093.82	Not seen in any published spectra	Charge exchange of H^+
NI 7	N	939.3	Contamination from N_2^+ Meinel (2-1)	Permitted $3s^2P$-$3p^2\ D^0$ No nightglow seen; auroral brightness ~200 R
NI 18	N	1,011.5	No auroral contamination	Permitted $3p^4\ D^0$-$3d^4F$; 5.0 kR in Vallance Jones & Gattinger (1976)
NI 3F	N	1,038.55	Slight contamination from N_2 1P (5,6) but otherwise clear of OH or auroral molecular bands	Forbidden (N^2D-N^2P); No nightglow seen; auroral 20 kR in Vallance Jones & Gattinger (1976)
O_2 IR A-band	O	1,268.7	-	~94 km altitude
NI	N	1,342.96	Clear of OH or auroral molecular bands	1 kR in Baker et al. (1977); 0.5 kR, Gattinger & Vallance Jones (1981)
OI	O	1,316.486	No auroral molecular contamination	Permitted $3p\ ^3P$-$4s\ ^3S^0$; 2.3 kR in Baker et al. (1977)
N_2^+ meinel 0-0	N_2	1,103.65 band origin	No OH contamination	Auroral activity; 212 kR in Baker et al. (1985)
N_2 1 positive 0-0	N_2	1,051.00 band origin	No OH contamination	Auroral activity; 77.1 kR in Baker et al. (1985)
OH 3-1 band P_1 (2)	OH	1,523.68	Little auroral contamination	Rotational temperature and intensity maps; 5–10 kR brightness
OH 3-1 band P_1 (4)	OH	1,542.79		Rotational temperature and intensity maps; 5–10 kR brightness

Typical auroral brightness are indicated relative to an IBC III aurora. The terms VJ & G and G & VJ refer to Vallance Jones & Gattinger (1976) and Gattinger & Vallance Jones (1981), respectively. These are all Air wavelengths. The phrase "Band Origin" does not denote a specific wavelength feature within a molecular band; rather, it denotes a numerical value representing the extrapolation to the minimum of the potential well.
SWIR, short-wave infrared.

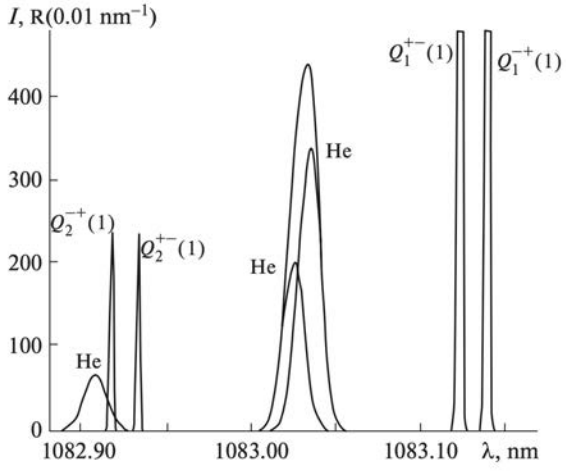

Fig. 4. Spectral structure illustrating the overlap of the three He 1,083 nm multiplet lines with the four Q components of the OH 5,2 band emission. The total He and OH emissions are estimated to be 1,000 R and 1,120 R, respectively.

treated images are then subtracted from the He 1,083 images after application of the P/Q branching ratios to determine the Q_1 and Q_2 images. A value for the 5–2 rotational temperature taken from the MSIS 00 model for a height of 87 km height (taken to be the peak height of the OH airglow profile) is used to determine the P/Q branching ratio for both Q_1 and Q_2 branch emissions. For a temperature of 180 K the $P_1(3)/Q_1$ and the $P_1(3)/Q_2$ ratios are ~0.7 and ~7.1, respectively. A synthetic spectra analysis (carried out by Dr. Charles Mutiso) shows that these two ratios are not sensitive to a change in the OH rotational temperature, with only a 2% increase and 8.9 % decrease seen for a 50 K shift in the temperature from 180 K to 230 K, respectively. The selection of this $P_1(3)$ OH emission line was based on the absence of any auroral contamination from molecular or atomic emissions.

An alternative approach relies on observing the combined 1,083 nm emissions near or past midnight when the He nightglow caused by resonance scattering is known to be weak (< 50 R). This ensures that the observed 1,083 nm signal (~1 kR) is dominated by the Q branch OH emissions. Simultaneous intensity measurement of the OH $P_1(3)$ and the composite 1,083 nm emissions will then enable the calculation of the desired ratios that can be used to correct and analyze He images collected earlier in the night.

These analysis approaches, which to our knowledge has not been previously described in imaging science literature, would need to be modeled and tested with pseudo-data to determine the range of error for both methods. The first

approach featuring the use of an OH filter is preferred as it relies on data to determine the separation of the He and OH emissions. The other approach is less preferable as it assumes that the He nightglow is non-existent at high solar zenith angles. Auroral spectra for this region found in Baker et al. (1977) and in Vallance Jones & Gattinger (1976) show that there is no significant auroral contamination from nitrogen band emissions.

3.3 Simulation of Expected SWIR Imaging Observations

To help evaluate the sensitivity of a SWIR imager like the Keo *Sentry-SWIR* to the emissions of Table 1, a forward model was developed to calculate the expected SWIR imager response. The quantum efficiency (QE) of an InGaAs sensor is nearly constant within the range of 80% to 85% across the spectral interval of 900–1,600 nm. The calculation of the signal-to-noise ratio (SNR), for each pixel is (Baumgardner et al. 2007):

$$S = \frac{\text{Signal}}{\text{Total noise}}$$

$$= I_S \times t_{exp} \times d_{pixel}^2 \times QE \,/\, \sqrt{\left(\left(Is + I_b\right) \times t_{exp} \times d_{pixel}^2 \times QE\right) + \left(\sigma_d \times t_{exp}\right) + \sigma_r^2}$$

where I_S is the incoming radiance (photons/μm^2/s), I_b is the background irradiance (photons/μm^2/s), t_{exp} is the exposure time (seconds), d_{pixel} is the pixel size (μm), σ_d is the dark current (electrons/pixel/s) and σ_r is the read noise (electrons/s/pixel). NIRvana dark current is specified by Teledyne Princeton Instruments as being 150 electrons/pixel/s when the sensor is cooled to –80°C and staring at a cold target held at –174°C. In the current use-case of looking at the sky through an observing dome, the actual dark current is found to be closer to 500 electrons/pixel/s. The readout noise is specified as 120 electrons/pixel. The spectral background signal is assumed to be 10 R/nm. The results are plotted in Fig. 5. The SNR determined for each emission of Table 1 was found to be greater than 20 for an exposure of 300 s, assuming a 100 R source brightness.

This model calculation demonstrates the feasibility of obtaining images of the spatial distribution of He, H, N, O, and N_2^+ atomic and molecular emissions seen in aurora and the He nightglow across a spatial extent of ~415 km for electron aurora at 120 km height, ~775 km for He aurora and proton aurora at ~225 km, and ~1,750 km for He nightglow at ~500 km. For He this corresponds to a latitudinal extent of ~12°, with a longitudinal extent of ~15° at 40° mid-latitude and ~27° at 65° high latitude. For nightglow observations of the OH layer at 87 km, this span would be ~300 km. In this spectral region, it is likely that imagery can be collected without significant contamination from OH in the case of auroral emissions, and without significant contamination from auroral emissions in the case of OH nightglow.

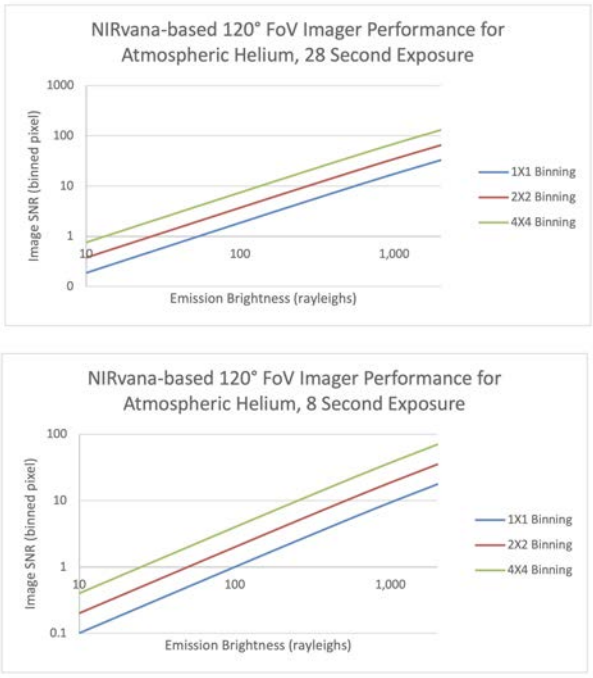

Fig. 5. Estimated signal-to-noise ratio (SNR) for four different binning schemes, assuming an exposure time of 28 s and 8 s, respectively (A 28 s exposure time facilitates a 30 s cadence, determined experimentally to be suitable for OH 3-1 band imaging in this wavelength region, allowing about 2 seconds for image readout and filter change between exposures.). FoV, field of view.

4. POTENTIAL SWIR IMAGER SCIENCE APPLICATIONS: AURORAL STUDIES

The following sections discuss the potential application of the Keo *Sentry-SWIR* – or any SWIR imager with comparable performance characteristics – to three distinct potential *auroral* research topics.

Section 4.1 deals with the topic of comparing the spatial morphology of helium, proton and electron auroras. The ability to study the spatial overlaps of these types of auroras promises to have implications regarding the evaluation of space weather effects in the thermosphere and exosphere. Section 4.2 suggests a method of searching for possible sub-auroral auroral forms such as STEVE, SAR-arcs and proton flashes (see reviews by Frey 2007; Gallardo-Lacourt et al. 2021). Finally, in Section 4.3, a method for searching for evidence of Alfvénic auroral activity is proposed. These examples are meant to illustrate the broad range of new science studies that are made possible through the recent

availability of deep-cooled SWIR imaging technology.

With reference to Table 1, the following list can be regarded as a proposed preliminary assortment of eight filters specifically targeted at studying SWIR auroras:

- Three filters to measure the He multiplet auroral emission at 1,083 nm, as described in Section 3.2.
- One filter to chase the proton auroral emission at the 1,281.8 nm Paschen β line.
- Two filters to measure the electron auroral emissions at the 0–0 "head" and "tail" of the N_2^+ Meinel system. See Section 4.3.
- One filter to measure the permitted transition emission of O at 1,316.5 nm, excited by energetic electron impact.
- One 'background continuum' filter centered on a region devoid of airglow/aurora emissions.

This proposed filter set, fully populating an 8-position filter wheel, provides the capability to observe images associated with three distinct types of auroras: (a) the electron aurora (the O permitted transition, and the two N_2^+ Meinel band emissions), (b) the proton aurora (the Paschen β emission), and (c) the helium aurora with the He auroral multiplet emission at 1,083 nm. The total time required to acquire these images is estimated to be between 5 to 10 minutes. As the Paschen β emission has never been detected before, nothing is known about its expected brightness, and thus required exposure times.

4.1 Proposed Application to Auroral and Polar Cusp Studies

Overlapping beams of incoming electrons and ions (He^{++}, He^+, H^+) into the upper atmosphere above the charge exchange region, see Fig. 6, can be expected to have different spatial footprint distributions. Unlike electrons, the incident proton beam is affected by lateral spreading due to the production of energetic neutral H atoms (Lorentzen & Moen 2000; Fang et al. 2005) within the region of charge exchange (~300–400 km). Lateral spreading should also apply to incoming streams of He^{++} and He^+, but to a lesser extent due to the greater mass of He relative to H. Also implied is that, given the same energy, He atoms would move more slowly than H. We note that ionization and stripping collisions caused by energetic He or H atoms impacting atmospheric neutral species would lead to emissions that are also caused by incoming electrons. The review papers by Reasoner (1973) and Prange (1978) both discuss the issue of the origin of energetic ions such as He^+ and He^{++} entering into the ionosphere. Reasoner found in a rocket ion mass spectrometer experiment that the observed

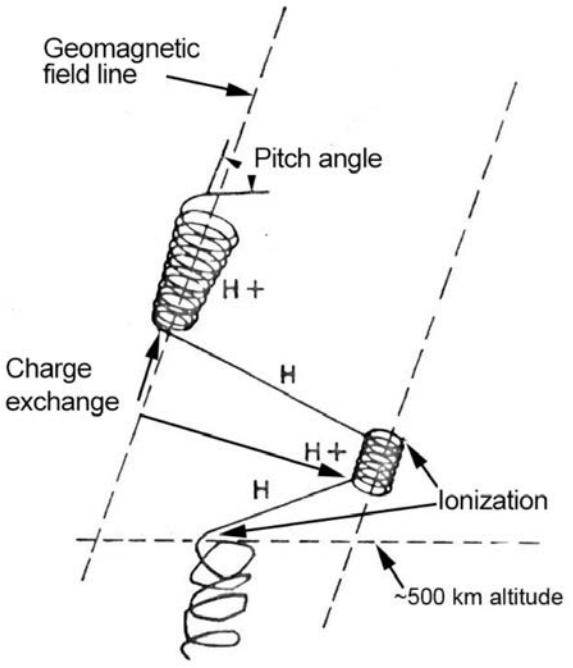

Fig. 6. Cartoon illustrating the effect of charge exchange followed by ionization or production of excited H atoms. Adapted from Egeland & Burke (2019) with CC-BY.

He^{++}/H^+ ratio was indeed similar to that observed in the solar wind. Prange's review suggested that the underlying physics as to how the He^{++} and He^+ particles are transferred from the solar wind to the ionosphere are quite complex. Clearly, this area of auroral physics deserves much more attention and extensive study. An imager observing at 1,083 nm offers an opportunity for ground-based studies to determine the spatial footprint of the energetic $He^{++}/He^+/He$ particle precipitation that is likely linked to the magnetotail origin where these particles are transferred from the solar wind into the ionosphere after acceleration by the local auroral acceleration region.

An ability to distinguish between the electron and proton components of auroral precipitation is essential to achieving a correct interpretation of auroral brightness in terms of ionospheric parameters such as ionization rate and conductivity (Galand et al. 2002; Galand & Lummerzheim 2004; Galand et al. 2004; Lanchester et al. 2011). Observations have shown that energetic electrons and protons do not interact with the upper atmosphere in the same way. Data from satellite-borne sensors show the existence of regions in the magnetosphere, conjugate to nightside proton aurorae, where a favorable environment for breaking the first adiabatic invariant allows keV protons to precipitate through the continual refilling of atmospheric loss cones. Moreover, space-borne imagers also show the

appearance of dayside hydrogen emissions in response to changes in either the solar wind's dynamic pressure or the interplanetary magnetic field's north–south component. It is thus necessary to carefully separate the electron and proton components of auroral particle precipitation to be able to correctly assess important space weather related ionospheric parameters such as conductivities, Joule heating, and changes in composition.

Fig. 7 illustrates an example of evening and morning latitudinal regions identified with proton precipitation relative to the nighttime electron auroral oval. In addition, as protons retain the large-scale structure more efficiently than electrons, imaging the proton aurora is an excellent probe for investigating magnetospheric sub-storms and magnetosphere-ionosphere coupling processes (e.g., Deehr & Lummerzheim 2001; Immel et al. 2002; Mende et al. 2003; Zhang et al. 2005; Lanchester et al. 2011). Moreover, protons can be the dominant energy source in the cusp and at the equatorward boundary of the dusk-side auroral oval (Creutzberg et al. 1988; Hardy et al. 1989; Galand et al. 2001). A recent review by Gallardo-Lacourt et al. (2021) presents an extended discussion regarding the magnetospheric physics underlying the separation of the electron and proton aurora morphology.

The conventional wisdom, as illustrated in Fig. 7, was that the proton aurora is located equatorward of electron aurora in the dusk-side of the auroral oval and poleward of electron aurora on the dawn-side. This view is incomplete, however, as shown by Zou et al. (2012), who found that the relative position of the electron and proton auroral boundaries depends significantly on the level of geomagnetic activity. The electron and proton boundaries were established by observing the 630 nm and $H_ß$ emissions using meridian-scanning photometers. Their results showed that during moderate and active periods, the electron aurora tended to lie equatorward of the proton aurora throughout the nightside region (20–03 MLT).

The interpretation of these findings provided by Zou et al. (2012) was that there is a dawn-dusk offset in the location of the auroral oval, with the proton aurora shifting toward pre-midnight and the electron aurora toward post-midnight. The penetration of the electron boundary equatorward of the proton precipitation across this magnetic local time (MLT) range had not been previously recognized. On the nightside, the proton aurora forms a band of diffuse aurora near the equatorward boundary of the electron auroral oval. This proton aurora is generally understood to be the projection of the central plasma sheet onto the ionosphere. Particles here have sufficient energy to cause enhanced luminosity in proton aurora following strong pitch angle scattering (likely caused by field-line curvature).

The contribution of helium to these spatial distributions of auroral forms within the auroral oval is still unknown, as ground-based all-sky imaging of auroral forms identified with He^{++} or He^{+} ion precipitation has not yet been achieved due to the lack of sensitivity (QE) of traditional silicon sensor technology (such as, CCDs) at the relevant wavelengths.

Some additional information is known regarding the role of energetic He^{+} and He^{++} particles in the cusp region. Henriksen et al. (1985) published the data for two sets of "daytime" 388.9 nm He spectra. These results, displayed in Fig. 8, showed that the behavior of this He emission brightness followed a bell-shaped curve that was anti-correlated with solar depression angle. The peak of this curve was seen during the noon period at the minimum solar depression angle of ~12°. Superimposed upon this smooth variation were occasional spikes of enhanced

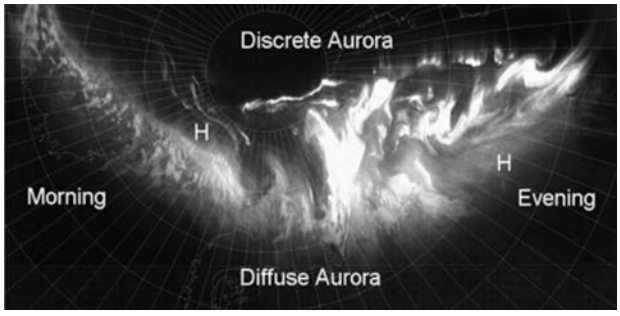

Fig. 7. This synoptic image of nightside aurora shows the relative location of the hydrogen emissions – marked with H – versus the oval, in both the morning and evening (from Egeland & Burke 2019, and also courtesy of Deehr & Lummerzheim, 2011). On the evening side the Balmer emissions are equatorward of the electron aurora, while on the morning side (left) the opposite is the case. Adapted from Egeland & Burke (2019) with CC-BY and Deehr & Lummerzheim (2011) with permission of American Geophysical Union.

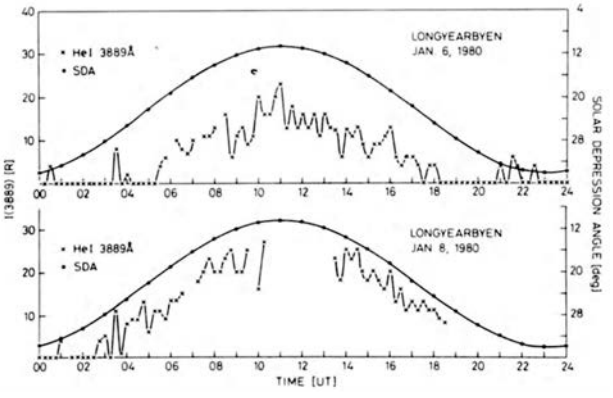

Fig. 8. Two examples of "daytime" brightness variation with the solar depression angle obtained from the analysis of Ebert-Fastie UV spectra of the He 388.9 nm emission.

brightness of a few rayleighs lasting a few minutes for each spike. These results were interpreted to suggest that the smooth variation was a result of resonance scattering because the He ^{2}S layer at 500 km was illuminated by the Sun. After considering several mechanisms, the authors claimed that the spikes were produced by incoming alpha particles that were transported into the cusp region by the solar wind. The analysis of polar cusp He images acquired in the SWIR spectral region would thus be of significant interest.

4.2 Midday Subauroral Patches, Dayside Detached Aurora, and Subauroral Proton Flashes

Adjacent to the auroral oval, there are often found against a background of diffuse auroral activity medium-scale auroral forms, 200 to 500 km in spatial extent. The appearance of these forms varies from spots to patches to elongated arcs of light emission. This phenomenology is summarized in the reviews by Frey (2007) and by Gallardo-Lacourt et al. (2021). Because these features are found poleward or equatorward of the oval, they are unlikely to be linked to the global auroral current system associated with the region of auroral activity. Accordingly, it is expected that such forms would have a different physical cause providing the increased flux or energy of precipitating electrons or ions. Some of these forms were first described using observations from the ISIS 2 and Viking satellites. The current availability of coincident solar wind data enables the integration of ground-based observations with a comprehensive perspective on solar wind-magnetosphere-ionosphere interactions, a synergy which has resulted in statistical investigations of large numbers of events and helped determine the external conditions that favored or suppressed a particular auroral form.

The application of a SWIR imager, such as the Keo *Sentry-SWIR*, to observe activity during geomagnetic storms at subauroral locations promises to enable the detection of SWIR emissions from these kinds of features during geomagnetic storm events, thus adding new insight into the underlying plasma physics.

4.3 A New Method for Distinguishing the Source of Electron Aurora Precipitation Morphology by an Optical Technique

This section describes a potential SWIR imager application that may well have a transformative outcome relating to ground-based optical studies of magnetospheric dynamics. Recently (cf. review by Keiling 2021), it has become evident that there are two distinct types of electron auroras: (1) direct precipitation of plasma sheet electrons that are accelerated by quasi-DC electric fields created by magnetic reconnection, and (2) ionospheric electrons that are accelerated by Alfvén waves. These two mechanisms are illustrated in Fig. 9.

In the former case, the auroral electron beams are mono-energetic with characteristic energies above 2 keV and have the relatively low fluxes and densities that are typical of the plasma sheet. In the latter case, ionospheric electrons are accelerated by Alfvén waves that are propagated from deep within the magnetosphere. The resultant auroral electrons in this case are of low energy, less than 2 keV, and with the high fluxes that are characteristic of ionospheric plasma densities. Thus, if there is a method of determining the penetration height of precipitating particles, then a distinction between these two auroral types may be made.

An approach to the problem of distinguishing between these two types of auroras has recently been discussed

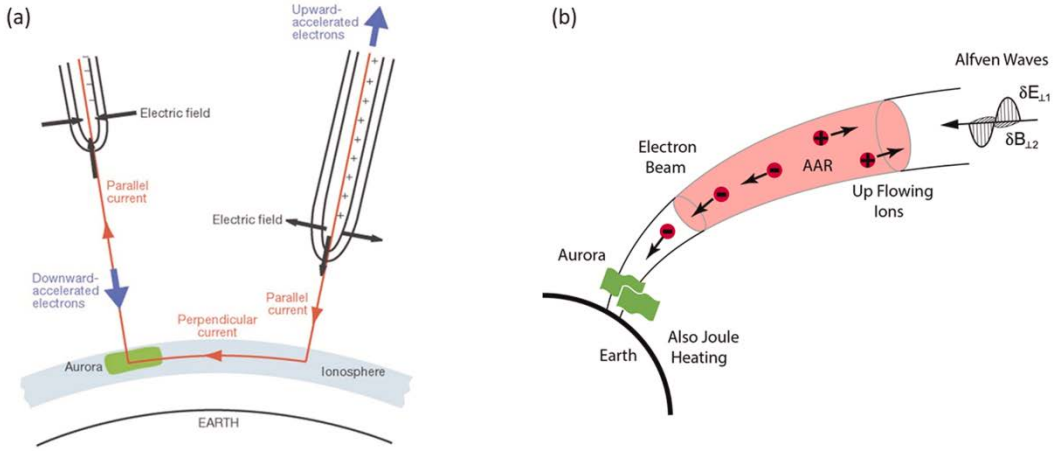

Fig. 9. Diagrams illustrating two possible acceleration mechanisms inside the auroral acceleration region. (a) Acceleration by quasi-static structures; (b) acceleration by Alfvén waves. Adapted from Keiling (2021) with CC-BY-ND.

in the literature (Mutiso et al. 2013; Mende 2016a, b). Alfvénic auroras have been identified in regions where magnetospheric reconfigurations take place, which might be the auroras associated with the auroral substorm onset, or with the auroral forms associated with poleward-expanding surges and boundary intensifications, or with dayside auroras [see reviews by Mende (2016a) and Keiling (2021)]. If Alfvénic auroras could be imaged and distinguished from other types of auroras, then it should be possible to apply ground-based optical imaging to map and monitor regions of significant magnetospheric dynamical activity. Thus, auroral imaging capable of distinguishing these two forms of dynamic electron auroras would be of great value in magnetospheric diagnostics.

As discussed in the review by Mende (2016b), these two types of electron auroras can be distinguished based on their electron energy spectra. Traditionally, remote sensing using optical measurement of electron energies was based on sensing the altitude of the aurora and comparing the intensity ratios of various spectral features emitted with different parent state lifetimes. Longer lifetime parent states have emissions that are attenuated by quenching in the lower atmosphere. Theoretically, from the ratio of spectral components of different quenching rates, the quenching altitude, and hence, the depth of particle penetration into the atmosphere, can be obtained. Unfortunately, this method is closely linked to the temporal response of the emissions. Thus, trying to use this method for studying highly dynamic electron auroras is intrinsically problematic, and the traditional methods of auroral energy discrimination applied to observations of electron aurora emissions are ineffective.

Measuring the rotational temperature, T_r, of the emitting species provides a means for making auroral height/electron characteristic energy measurements (Hunten et al. 1963; Jokiaho et al. 2008; Mutiso et al. 2013; Mende 2016b; Nishiyama et al. 2021). The temperature of the atmosphere at 100 km altitude is about 200 K, while at 200 km it might be ~800 K or higher. Therefore, the T_r measurement of a molecular auroral emission band combined with the MSIS 2.0 empirical model should be able to provide measurements of the auroral height, and thereby an estimate of the electron penetration depth. This concept is discussed in detail by Hunten et al. (1963) with an updated version presented by Mende (2016b), who applied this technique to the 0–1 band of the First Negative System of N_2^+ at 427.8 nm. Fig. 10 illustrates the wavelength positions chosen relative to the molecular band structure for two filter passbands for three T_r values. It can be seen how the intensity ratio would increase with an increase in

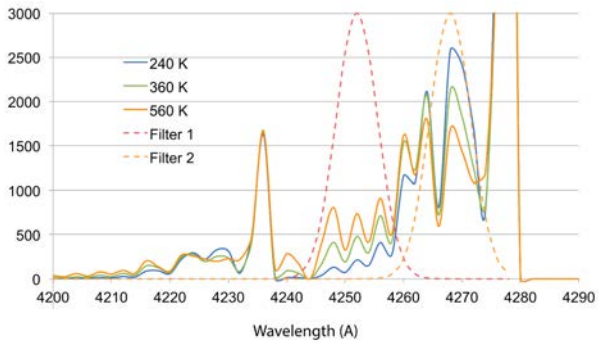

Fig. 10. Synthetic spectral distributions of the 0-1 N_2^+ 1NG band emission calculated for a range of rotational temperature from 240 K to 560 K. The transmission profiles (dashed curves) for the "head" and "tail" band emissions located at 427.0 nm and 425.5 nm, respectively, are also plotted. Adapted from Mende (2016b) with CC-BY-NC-ND.

T_r. In this work as well as that of Hunten et al. (1963), who observed the 0-0 band emission of N_2^+ at 391.4 nm, the ratio of measured photometer signals for auroral observations is obtained using two filters with wavelengths isolating the "head" and "tail" emissions. The observed ratio is compared with the set of predicted ratios for a range of T_r values computed from synthetic spectral analysis of the 0–1 band spectral profile convolved with measured filter transmission profiles for the two wavelengths. The interpolation of the observed ratio to the range of calculated ratios provides a reasonably accurate estimate of T_r.

Comparing the inferred 0–1 N_2^+ rotational temperature to the MSIS temperature profile for the range between 100 and 200 km would extract an altitude for which the auroral penetration depth and precipitating particle characteristic energy can be inferred. In the case of the 0–0 N_2^+ Meinel band at 1,103.0 nm, the two head and tail emissions selected would be very bright (typically greater than 20 kR). Contamination by other nightglow or auroral emission sources would be minimal in this spectral range. Thus, each of the two images required for a SWIR imaging application could be observed with a fairly short exposure time of a few seconds.

It is important that the imager be fielded near an existing incoherent scatter radar (ISR) for the purposes of testing and calibrating the technique. The ISR generates ionization height profiles that can be directly compared to the height derived from the optical Meinel band emission ratios as observed by the SWIR imager. Previous efforts by Mutiso et al. (2013) using this technique combined with radar measurements were quite successful.

In conclusion, using one pair of (temporally and spectrally close) images and the model of calculated ratios, based upon synthetic spectra for a range of rotational

temperatures, the auroral height and characteristic energy of precipitating electrons may be mapped across the observed spatial region (300 to 500 km in horizontal extent, with a horizontal resolution of tens of km depending upon the pixel binning strategy employed). Such a SWIR optical imaging technique should enable one to, e.g., quantify the role of Alfvén waves in creating phenomena such as poleward boundary intensification, substorm onset, and poleward expanding surges. Other examples include rays (Ivchenko et al. 2005), vortices (Chaston et al. 2010), poleward boundary intensifications (Mella et al. 2011), field line resonances (Liou & Takahashi 2013), and the poleward border of auroral surges (Mende et al. 2003). These features taken together are defined by Keiling to make up the Alfvén auroral oval.

5. POTENTIAL SWIR IMAGER SCIENCE APPLICATIONS: AIRGLOW STUDIES

The following subsections discuss the application of the Keo *Sentry-SWIR* – or any imager with similar performance characteristics – to two distinct potential *airglow* research topics.

Section 5.1 delves into the study of mesosphere dynamics by means of generating thermal maps and observing OH intensity distributions. The instrument has already been successfully applied to this application (Dalin et al. 2024). Section 5.2 proposes studying the short-term (hours) and long-term (seasonal) variability behavior of He and OH nightglow.

With reference to Table 1, the following is a suggested provisional selection of eight filters suitable for SWIR airglow studies:

- Three filters for measuring the OH rotational temperature and OH intensities. The two filters sample the $P_1(2)$ and $P_1(4)$ brightness of the 4–1 band, and the third filter sample the background continuum. This application is described in Section 5.1.
- Three filters to measure the He nightglow multiplet at 1,083 nm, using the technique described in Section 3.2. One suggested airglow application is described below, in Section 5.2.
- One (1) 1,268.7 nm O_2 airglow filter.
- One (1) low-emissivity filter, described in Section 2.1, used to obtain a measurement of the infrared radiation produced by the instrument itself, and its environment.

The cadence is expected to be ~10 minutes for the full filter set. The instrument can be outfitted with other filters in the future, enabling "discovery science" as scientific understanding advances.

5.1 Optical Temperature Measurements of the Mesosphere and Thermosphere

GWs in the Earth's atmosphere are launched from many sources such as wind flow over mountains and jet stream adjustments (Xu et al. 2021, and references therein) as well as by tropospheric deep convection such as thunderstorms and tropical cyclones (Alexander et al. 1995; Fritts & Joan Alexander 2003; Alexander et al. 2010; Hoffmann & Alexander 2010). These waves tend to break at the turbopause altitude of ~105 km. For altitudes within the OH volume emission profiles most GW events are just beginning to undergo dissipation near the 85–87 km peak altitude of the OH nightglow. Clearly, obtaining a two-dimensional map of temperature and images of intensity wave structures with such a large field of view, covering 300 km, and high cadence would represent a powerful tool for studying mesosphere dynamics. An overview of the results that might be obtained from such maps of rotational temperatures and OH band intensities can be found in the work by Schmidt et al. (2013) and Wachter et al. (2015). These papers examined the statistics of the 61 wave events identified over the course of six months of observations. GW periodicities for the mesosphere region were found to be typically within the range of 2 to 4 hours. Inertial GWs and long period GWs showed much longer periods, perhaps 7 to 9 hours.

Nighttime imaging of SWIR OH emission in the upper mesosphere/lower thermosphere region around 87 km altitude have proven useful over the past decade in providing large-area remote sensing of mesospheric temperatures, as well as intensity maps showing the propagation and dissipation of atmospheric GWs and small-scale features known as ripples. The intensity ratio of OH rotational emissions of $P_1(2)$ at 1,523.68 nm to $P_1(4)$ at 1,542.79 nm is central to the measurement of mesospheric temperature. These two emissions display substantial luminosity, with a brightness ranging from 5 to 10 kR (Nishiyama et al. 2021), allowing a SWIR imager to capture mesoscale imagery at a high ratio of signal to noise.

The technique of comparing the brightness of two or more emission lines from hydroxyl in the region around 87 km altitude was pioneered by Meriwether (1975) and is the basis for the Mesospheric Temperature Mapper (MTM) (Taylor et al. 2001) and the AMTM (Pautet et al. 2014). Other optical methods for determining the temperature of this region of the atmosphere are presented in a comparison

table by Pautet et al. (2014), and have similar measurement errors, but significantly smaller fields of view. These instruments include a Fourier spectrometer, a Fourier transform spectrometer, a Michelson interferometer, and a more traditional spectrometer.

Fig. 11 (adapted from Trondsen et al. 2021) shows the filter functions of the two OH channels and the 1,521.0 nm background continuum, channel, superposed on a synthetic spectrum (courtesy of Philippe Rousselot, University of Franche-Comté). Filter bandwidths are 1.0 nm FWHM.

Fig. 12 shows raw images acquired using a Keo *Sentry-SWIR* (Trondsen et al. 2021). The images presented here have 10 second integration periods for the three sky channels (and the dark frame, not shown). Note that the background channel exhibits minimal sky emission within its spectral bandwidth.

Data inversion from these raw images to the creation of a temperature map is a multi-step process involving dark subtraction, background subtraction, field flattening, conversion to absolute brightness and finally calculation of the sky temperature from the brightness ratio. The process

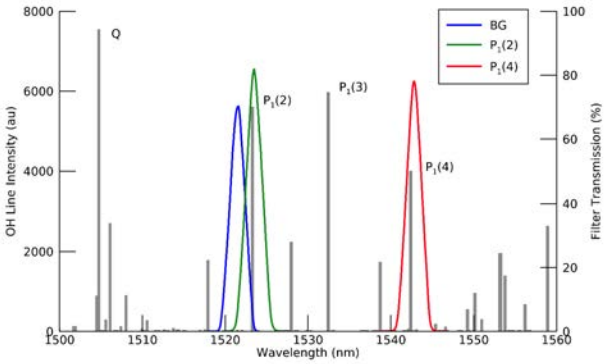

Fig. 11. Examples of filter transmission profiles for the OH temperature mapping application. Peak transmission is typically 70% to 80%.

of dark-frame subtraction involves capturing dark frames, which are subsequently used to eliminate both the fixed pattern noise of the InGaAs photodiode array (manifesting as vertical streaks, as seen in the raw data of Fig. 12) and other non-signal counts present in the pixels. The process of background subtraction, performed in spectral density space, is used to remove the broadband continuum emission

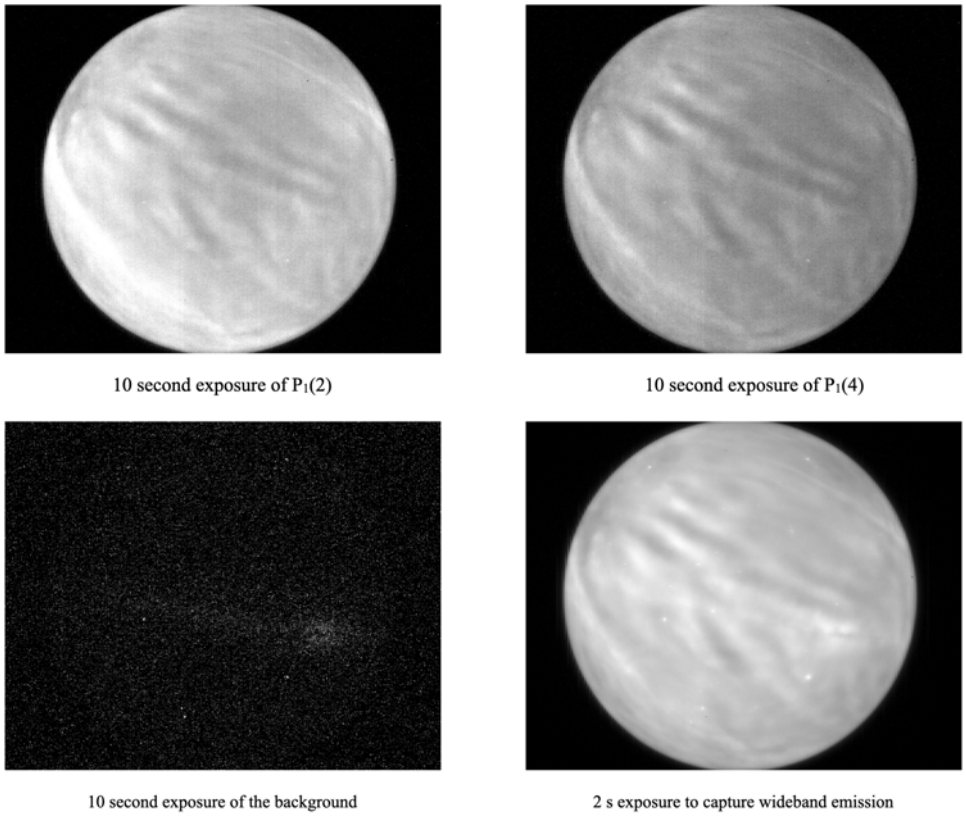

Fig. 12. Raw images from the two OH channels of OH $P_1(2)$ at 1,523.68 nm and $P_1(4)$ at 1,542.79 nm, as well as the background continuum channel at 1,521.0 nm and a 900–1,700 nm wideband filter.

present within the spectral passband of the OH filters. The field flattening step is required to account for vignetting and intra-filter variation in transmission across the surface of narrowband filters at the OH emission wavelengths. The process of converting to absolute units can subsequently be carried out, followed by the calculation of the ratio of hydroxyl line emission intensities, and finally the temperature of the OH layer can be estimated using the following equation (from Pautet et al. 2014):

$$T_r = 259.58 / \ln(2.644\,R),$$

where R is the brightness ratio of $P_1(2)$ to $P_1(4)$.

Note that Dalin et al. (2024) uses a factor of 2.658 instead of 2.644, as they corrected the equation for newly estimated Einstein A-coefficients for the OH(3-1) band at $P_1(2)$ and $P_1(4)$ lines, as calculated by Brooke et al. (2016). This results in a 0.7 K–1.5 K temperature difference between Pautet et al. (2014) and Dalin et al. (2024) temperature estimations, for a typical range of winter temperatures in the mesopause.

Fig. 13, from Dalin et al. (2024) shows an example of the resulting corrected temperature map, capturing spatial scales on the order of kilometers.

Dalin et al. (2024) also employed a 1,268.7 nm filter to measure airglow emissions from the O_2 IR A-band, originating at the slightly higher altitude of ~94 km. This technique allows mapping GW disturbances in the horizontal as well as the vertical dimension in the

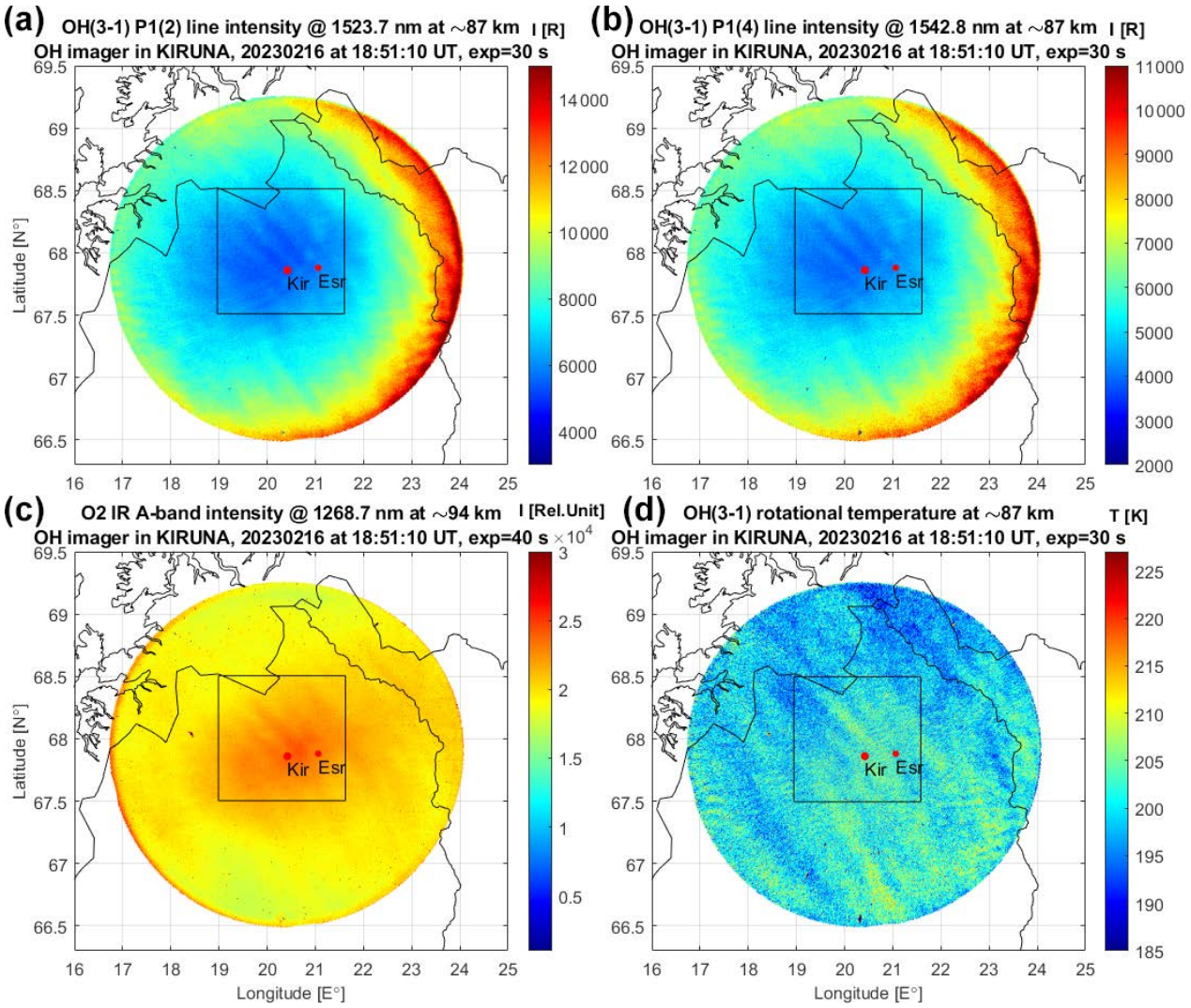

Fig. 13. Maps of airglow intensities and temperature obtained by the OH imager on 16 February 2023. (a) Intensity in the Rayleigh of the OH(3-1) $P_1(2)$ line at 1,523.7 nm. (b) Intensity in the Rayleigh of the OH(3-1) $P_1(4)$ line at 1,542.8 nm. (c) Intensity in relative units of the O_2 IR A-band at 1,268.7 nm. (d) OH(3-1) rotational temperature estimated by the brightness ratio of the two OH(3-1) emission lines. Adapted from Dalin et al. (2024) with CC-BY.

mesopause region.

5.2 Studying the He Nightglow Behavior Regarding Seasonal, Nocturnal, and Short-Term Variability

The question of the He composition distribution at low Earth orbit (LEO) altitudes has attracted considerable attention in recent years (Thayer et al. 2012; Sutton et al. 2015). This renewed attention can be attributed in part to the fact that the production of the He winter bulge contributes substantially toward the uncertainty in total atmospheric density estimates for LEO altitudes in the polar regions. Fig. 14 illustrates an example of the winter He bulge seen in OGO-6 data obtained at 240 km, in contrast to N_2, O, and Ar densities (Reber 1976). The variation in He density from the summer pole to the winter pole is about an order of magnitude. Also of interest in this figure is the sharp reduction of the He density resulting from a moderate geomagnetic disturbance. The origin of the He winter bulge has been attributed to a global circulation cellular system featuring upwelling in the central polar region in the winter hemisphere and downwelling in the summer hemisphere (Reber & Hays 1973; Reber 1976; Sutton et al. 2015).

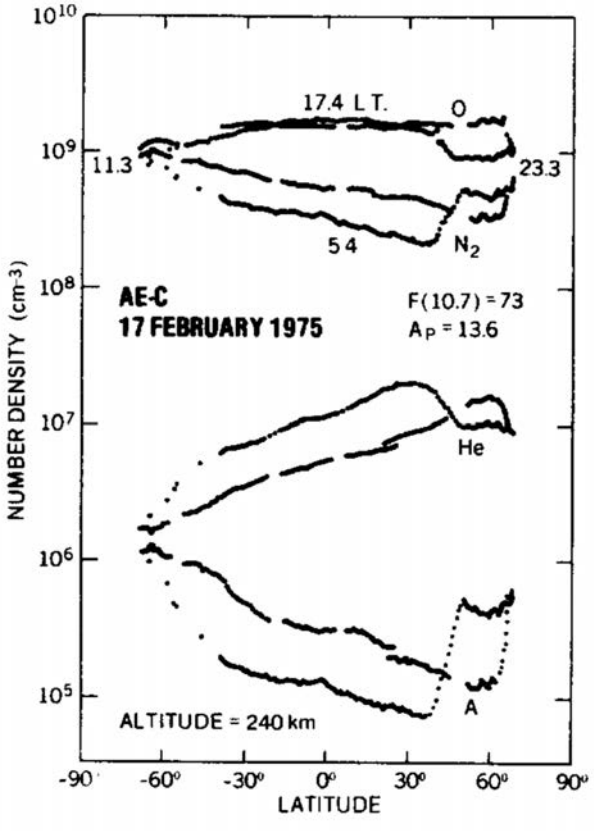

Fig. 14. OGO-6 density measurements at 240 km plotted as a function of altitude for N_2, O, Ar, and He for orbital passes during a quiet and a moderately active period.

Waldrop et al. (2005), using Arecibo ISR composition data and models for the topside photochemistry and production by photoelectron impact, calculated the metastable He(2^3S) density profile for morning twilight at a solar zenith angle of 110°. These calculations also compensated for losses caused by the processes of radiative decay, photoionization, and Penning ionization. It was found that the He(2^3S) vertical distribution has a broad peak within the height range of 400–800 km. The nightglow 1,083 nm He triplet emissions are generated by resonant scattering of the 1,083 nm solar photons by the metastable He atoms within this layer.

The He 1,083 nm nighttime brightness variation is key to the proposed SWIR measurements. It is well known that there is likely to be – especially for the solar maximum period – continual excitation of this helium 1,083 nm emission throughout the night, but with enhanced brightness near twilight caused by photoelectron impact (as also used in Gerrard et al. (1997) for He-LIDAR calculations). The intensity variation found in these calculations for a 85°–130° range of solar zenith angles was typically from 1,500 to 2,000 R in twilight to 30 to 50 R near midnight, as shown in the top panel of Fig. 15 (Waldrop et al. 2005). The bottom panel in Fig. 15 shows the variation of the production by the recombination and photoelectron impact sources, including the flux from the conjugate hemisphere.

The span of the He nightglow images of 1,750 km, as acquired by a SWIR imager with 120° field of view, would correspond to a fairly large range of about 12° in latitude.

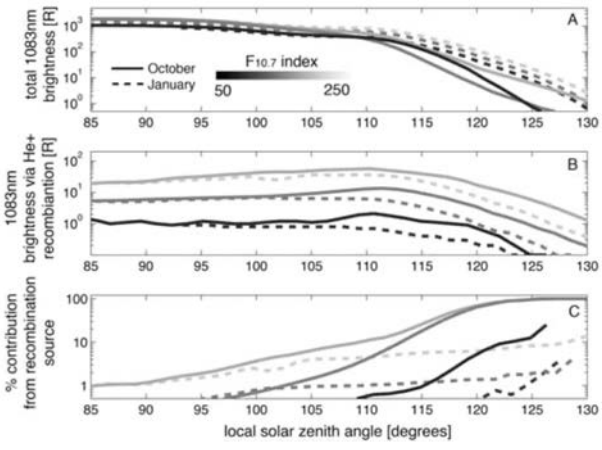

Fig. 15. Calculation of the He 1,083 nm brightness variation with local solar zenith angle for October and January months. The lines' gray tone represents the solar $F_{10.7}$ index used in the model calculation with the dark curve representing weak solar activity and the light gray curve the solar maximum (see gray color bar). Results for October and January are plotted as solid lines and dashed lines, respectively.

This implies that the SWIR imager should be able to observe variations in the meridional gradient in the exospheric He brightness over a period of hours to several nights. Interpretation of these results will likely require comparisons of TIEGCM model predictions with case studies of He brightness data for a range of $F_{10.7}$ and Kp indices.

In summary, imaging the He airglow during twilight for solar zenith angles within the range of 100°–130° promises to enable the determination of the He winter bulge dynamics with potentially high precision at LEO heights, of particular interest to space weather studies as applied to orbital drag considerations.

6. CONCLUSIONS

The extension of geospace imaging into the SWIR portion of the spectrum (1.0–1.7 μm) offers new avenues for space weather exploration and holds the potential to contribute to a deeper understanding of the geospace environment. The versatility of SWIR imaging may also improve diagnostic measurements in support of existing instrumentation and facilities.

This paper specifically introduces the Keo *Sentry-SWIR* imager and its successful deployment in studying mesosphere dynamics, emphasizing the potential of SWIR imagers in general for a wide range of applications, including exploring energetic particle deposition distributions, identifying sub-auroral phenomena, investigating Alfvénic auroras, and exploring helium nightglow brightness variability.

It should be noted that the emission intensity of helium is closely tied to the level of solar activity (Shefov et al. 2009). Currently, solar activity is increasing, and there is a projected peak expected later this year. This makes the years 2024/2025 particularly favorable for helium brightness studies.

ACKNOWLEDGMENTS

Trond S. Trondsen wishes to thank Stephen Mende for valuable discussions, going back to 2011, on the topic of determining the source of electron aurora precipitation by optical techniques. John Meriwether wishes to acknowledge the 2023 Defense University Research Instrumentation Program (DURIP) for funding support (FA9550-23-1-0412) of the acquisition of the Keo *Sentry-SWIR* imager to the Center for Solar-Terrestrial Research at the New Jersey Institute of Technology. We thank Charles Mutiso and Matthew Zettergren (Embry-Riddle Aeronautical University) for their helpful comments on the application of SWIR imaging to the study of auroral physics.

ORCIDs

Trond S. Trondsen https://orcid.org/0000-0002-9538-1832
John Meriwether https://orcid.org/0000-0002-2523-1011
Craig Unick https://orcid.org/0000-0002-3006-3198
Andrew Gerrard https://orcid.org/0000-0002-9626-2085
Matthew Cooper https://orcid.org/0000-0001-6137-8814
Devin Wyatt https://orcid.org/0000-0002-5078-9500

REFERENCES

Alexander MJ, Geller M, McLandress C, Polavarapu S, Preusse P, et al., Recent developments in gravity-wave effects in climate models and the global distribution of gravity-wave momentum flux from observations and models, Q. J. R. Meteorol. Soc. 136, 1103-1124 (2010). https://doi.org/10.1002/qj.637

Alexander MJ, Holton JR, Durran DR, The gravity wave response above deep convection in a squall line simulation, J. Atmos. Sci. 52, 2212-2226 (1995). https://doi.org/10.1175/1520-0469(1995)052<2212:TGWRAD>2.0.CO;2

Baker D, Pendleton W Jr, Steed A, Huppi R, Stair AT Jr, Near-infrared spectrum of an aurora, J. Geophys. Res. 82, 1601-1609 (1977). https://doi.org/10.1029/JA082i010p01601

Baker DJ, Steed AJ, Ware GA, Offermann D, Lange G, et al., Ground-based atmospheric infrared and visible emission measurements, J. Atmos. Terr. Phys. 47, 133-145 (1985). https://doi.org/10.1016/0021-9169(85)90129-1

Baumgardner JL, Flynn B, Mendillo MJ, Monochromatic imaging instrumentation for applications in aeronomy of the Earth and planets, Opt. Eng. 32, 3028-3032 (1993). https://doi.org/10.1117/12.149194

Baumgardner J, Wroten J, Semeter J, Kozyra J, Buonsanto M, et al., A very bright SAR arc: implications for extreme magnetosphere-ionosphere coupling, Ann. Geophys. 25, 2593-2608 (2007). https://doi.org/10.5194/angeo-25-2593-2007

Beedle JMH, Rura CE, Simpson DG, Cohen HI, Moraes Filho VP, et al., A user's guide to the magnetically connected space weather system: a brief review, Front. Astron. Space Sci. 8:786308 (2022). https://doi.org/10.3389/fspas.2021.786308

Brooke JSA, Bernath PF, Western CM, Sneden C, Afşar M, et al., Line strengths of rovibrational and rotational transitions in the $X^2\prod$ ground state of OH, J. Quant. Spectrosc. Radiat. Transf. 168, 142-157 (2016). https://doi.org/10.1016/j.jqsrt.

2015.07.021
Bosqued JM, Ion precipitation into the ionosphere during geomagnetic storms, Adv. Space Res. 5, 179-191 (1985). https://doi.org/10.1016/0273-1177(85)90136-X
Chaston CC, Seki K, Sakanoi T, Asamura K, Hirahara M, Motion of aurorae, Geophys. Res. Lett. 37, L08104 (2010). https://doi.org/10.1029/2009GL042117
Creutzberg F, Gattinger RL, Harris FR, Wozniak S, Vallance Jones A, Auroral studies with a chain of meridian scanning photometers, 2, mean distributions of proton and electron aurora as a function of magnetic activity, J. Geophys. Res. 93, 14591-14601 (1988). https://doi.org/10.1029/JA093iA12p14591
Dalin P, Brändström U, Kero J, Voelger P, Nishiyama T, et al., A novel infrared imager for studies of hydroxyl and oxygen nightglow emissions in the mesopause above northern Scandinavia, Atmos. Meas. Tech. 17, 1561-1576 (2024). https://doi.org/10.5194/amt-17-1561-2024
Deehr C, Lummerzheim D, Ground-based optical observations of hydrogen emission in the auroral substorm, J. Geophys. Res. 106, 33-44 (2001). https://doi.org/10.1029/2000JA002010
Eather RH, Auroral proton precipitation and hydrogen emissions, Rev. Geophys. 5, 207-285 (1967). https://doi.org/10.1029/RG005i003p00207
Eather RH, Advances in magnetospheric physics: aurora, Rev. Geophys. 13, 925-943 (1975). https://doi.org/10.1029/RG013i003p00925
Eather RH, Results from Antarctic optical studies, Rev. Geophys. 26, 579-590 (1988). https://doi.org/10.1029/RG026i003p00579
Egeland A, Burke WJ, Auroral hydrogen emissions: a historical survey, Hist. Geo Space Sci. 10, 201-213 (2019). https://doi.org/10.5194/hgss-10-201-2019
Fang X, Liemohn MW, Kozyra JU, Solomon SC, Study of the proton arc spreading effect on primary ionization rates, J. Geophys. Res. 110, A07302 (2005). https://doi.org/10.1029/2004JA010915
Frey HU, Localized aurora beyond the auroral oval, Rev. Geophys. 45, RG1003 (2007). https://doi.org/10.1029/2005RG000174
Fritts DC, Joan Alexander M, Gravity wave dynamics and effects in the middle atmosphere, Rev. Geophys. 41, 1003 (2003). https://doi.org/10.1029/2001rg000106
Galand M, Introduction to special section: proton precipitation into the atmosphere, J. Geophys. Res. 106, 1-6 (2001). https://doi.org/10.1029/2000JA002015
Galand M, Lummerzheim D, Stephan AW, Bush BC, Chakrabarti S, Electron and proton aurora observed spectroscopically in the far ultraviolet, J. Geophys. Res. 107, 1-14 (2002). https://doi.org/10.1029/2001JA000235
Galand M, Lummerzheim D, Contribution of proton precipitation to space-based auroral FUV observations, J. Geophys. Res. 109, A03307 (2004). https://doi.org/10.1029/2003JA010321
Galand M, Baumgardner J, Pallamraju D, Chakrabarti S, Løvhaug UP, et al., Spectral imaging of proton aurora and twilight at Tromsø, Norway, J. Geophys. Res. 109, A07305 (2004). https://doi.org/10.1029/2003JA010033
Galand M, Chakrabarti S, Proton aurora observed from the ground, J. Atmos. Sol. Terr. Phys. 68, 1488-1501 (2006). https://doi.org/10.1016/j.jastp.2005.04.013
Galand M, Fuller-Rowell TJ, Codrescu MV, Response of the upper atmosphere to auroral protons, J. Geophys. Res. 106, 127-139 (2001). https://doi.org/10.1029/2000JA002009
Gallardo-Lacourt B, Frey HU, Martinis C, Proton aurora and optical emissions in the subauroral region, Space Sci. Rev. 217, 10 (2021). https://doi.org/10.1007/s11214-020-00776-6
Gattinger RL, Vallance Jones A, Quantitative spectroscopy of the aurora. V. The spectrum of strong aurora between 10 000 and 16 000 Å, Can. J. Phys. 59, 480-487 (1981). https://doi.org/10.1139/p81-059
Gerrard AJ, Kane TJ, Meisel DD, Thayer JP, Kerr RB, Investigation of a resonance Lidar for measurement of thermospheric metastable helium, J. Atmos. Sol. Terr. Phys. 59, 2023-2035 (1997). https://doi.org/10.1016/S1364-6826(97)00046-1
Hardy DA, Gussenhoven MS, Brautigam D, A statistical model of auroral ion precipitation, J. Geophys. Res. 94, 370-392 (1989). https://doi.org/10.1029/JA094iA01p00370
Henriksen K, Stamnes K, Deehr CS, Sivjee GG, The HeI 3889Å line in polar cleft spectra, in the Polar Cusp, eds. Holtet JA, Egeland A (D. Reidel Publishing Company, Dordrecht, 1985), 127-135.
Hoffmann L, Alexander MJ, Occurrence frequency of convective gravity waves during the North American thunderstorm season, J. Geophys. Res. 115, D20111 (2010). https://doi.org/10.1029/2010jd014401
Hunten DM, Rawson EG, Walker JK, Rapid measurement of N_2^+ rotational temperatures in aurora, Can. J. Phys. 41, 258-270 (1963). https://doi.org/10.1139/p63-032
Immel TJ, Mende SB, Frey HU, Peticolas LM, Carlson CW, et al., Precipitation of auroral protons in detached arcs, Geophys. Res. Lett. 29, 1519 (2002). https://doi.org/10.1029/2001GL013847
Ivchenko N, Blixt EM, Lanchester BS, Multispectral observations of auroral rays and curls, Geophys. Res. Lett. 32, L18106 (2005). https://doi.org/10.1029/2005GL022650
Jokiaho O, Lanchester BS, Ivchenko N, Daniell GJ, Miller LCH, et al., Rotational temperature of N_2^+ (0,2) ions from spectrographic measurements used to infer the energy of precipitation in different auroral forms and compared with radar measurements, Ann. Geophys. 26, 853-866 (2008). https://doi.org/10.5194/angeo-26-853-2008
Keiling A, The dynamics of the Alfvénic oval, J. Atmos. Sol. Terr.

Phys. 219, 105616 (2021). https://doi.org/10.1016/j.jastp.2021.105616

Lanchester B, Jokiaho OP, Galand M, Ivchenko N, Lummerzheim D, et al., Separating and quantifying ionospheric responses to proton and electron precipitation over Svalbard, J. Geophys. Res. 116, A09322 (2011). https://doi.org/10.1029/2011JA016474

Liou K, Takahashi K, Observations of field line resonance with global auroral images, J. Atmos. Sol. Terr. Phys. 105–106, 152-159 (2013). https://doi.org/10.1016/j.jastp.2013.09.005

Lorentzen DA, Moen J, Auroral proton and electron signatures in the dayside aurora, J. Geophys. Res. 105, 12733-12745 (2000). https://doi.org/10.1029/1999JA900405

Martinis C, Baumgardner J, Wroten J, Mendillo M, All-sky-imaging capabilities for ionospheric space weather research using geomagnetic conjugate point observing sites, Adv. Space Res. 61, 1636-1651 (2018). https://doi.org/10.1016/j.asr.2017.07.021

Mella MR, Lynch KA, Hampton DL, Dahlgren H, Kintner PM, et al., Sounding rocket study of two sequential auroral poleward boundary intensifications, J. Geophys. Res. 116, A00K18 (2011). https://doi.org/10.1029/2011JA016428

Mende SB, Frey HU, Morsony BJ, Immel TJ, Statistical behavior of proton and electron auroras during substorms, J. Geophys. Res. 108, 1339 (2003). https://doi.org/10.1029/2002JA009751

Mende SB, Observing the magnetosphere through global auroral imaging: 1. observables, J. Geophys. Res. Space Phys. 121, 10623-10637 (2016a). https://doi.org/10.1002/2016JA022558

Mende SB, Observing the magnetosphere through global auroral imaging: 2. observing techniques, J. Geophys. Res. Space Phys. 121, 10638-10660 (2016b). https://doi.org/10.1002/2016JA022607

Meriwether JW, High latitude airglow observations of correlated short-term fluctuations in the hydroxyl Meinel 8-3 band intensity and rotational temperature, Planet. Space Sci. 23, 1211-1221 (1975). https://doi.org/10.1016/0032-0633(75)90170-1

Mutiso CK, Zettergren MD, Hughes JM, Sivjee GG, Thermospheric neutral temperatures derived from charge-exchange produced N_2^+ Meinel (1,0) rotational distributions, Ann. Geophys. 31, 463-471 (2013). https://doi.org/10.5194/angeo-31-463-2013

Nishiyama T, Taguchi M, Suzuki H, Dalin P, Ogawa Y, et al., Temporal evolutions of N_2^+ Meinel (1,2) band near 1.5 μm associated with aurora breakup and their effects on mesopause temperature estimations from OH Meinel (3,1) band, Earth Planets Space 73, 30 (2021). https://doi.org/10.1186/s40623-021-01360-0

Pautet PD, Taylor MJ, Pendleton WR, Zhao Y, Yuan T, et al., Advanced mesospheric temperature mapper for high-latitude airglow studies, Appl. Opt. 53, 5934-5943 (2014). https://doi.org/10.1364/AO.53.005934

Prange R, Energetic (keV) ions of ionospheric origin in the magnetosphere. A review. Ann. Geophys. 34, 187-213 (1978).

Reasoner DL, Auroral helium precipitation, Rev. Geophys. 11, 169-180 (1973) https://doi.org/10.1029/RG011i001p00169

Reber CA, Hays PB, Thermospheric wind effects on the distribution of helium and argon in the Earth's upper atmosphere, J. Geophys. Res. 78, 2977-2991 (1973). https://doi.org/10.1029/JA078i016p02977

Reber CA, Dynamical effects in the distribution of helium in the thermosphere, J. Atmos. Terr. Phys. 38, 829-840 (1976). https://doi.org/10.1016/0021-9169(76)90023-4

Rousselot P, Lidman C, Cuby JG, Moreels G, Monnet G, Night-sky spectral atlas of OH emission lines in the near-infrared, Astron. Astrophys. 354, 1134-1150 (2000).

Saum KA, Benesch WM, Infrared electronic emission spectrum of nitrogen, Appl. Opt. 9, 195-200 (1970a). https://doi.org/10.1364/AO.9.000195

Saum KA, Benesch WM, Infrared electronic emission spectrum of oxygen, Appl. Opt. 9, 1419-1423 (1970b). https://doi.org/10.1364/AO.9.001419

Schmidt C, Höppner K, Bittner M, A ground-based spectrometer equipped with an InGaAs array for routine observations of OH(3-1) rotational temperatures in the mesopause region, J. Atmos. Sol. Terr. Phys. 102, 125-139 (2013). https://doi.org/10.1016/j.jastp.2013.05.001

Shefov NN, Semenov AI, Yurchenko OT, Empirical model of variations in the helium 1083 nm emission. 1. Intensity. Geomagn. Aeron. 49, 93-103 (2009). https://doi.org/10.1134/S0016793209010137

Shefov NN, Semenov AI, Helium in the terrestrial upper atmosphere: spatial and temporal distribution of its emission in the infrared spectral region, in helium: characteristics, compounds, and applications (Nova Science Publishers, Hauppauge, 2011), 1-50.

Sutton EK, Thayer JP, Wang W, Solomon SC, Liu X, et al., A self-consistent model of helium in the thermosphere, J. Geophys. Res. Space Phys. 120, 6884-6900 (2015). https://doi.org/10.1002/2015JA021223

Taylor MJ, Gardner LC, Pendleton WR Jr, Long-period wave signatures in mesospheric OH Meinel (6,2) band intensity and rotational temperature at mid-latitudes, Adv. Space Res. 27, 1171-1179 (2001). https://doi.org/10.1016/S0273-1177(01)00153-3

Thayer JP, Liu X, Lei J, Pilinski M, Burns AG, The impact of helium on thermosphere mass density response to geomagnetic activity during the recent solar minimum, J. Geophys. Res. 117, A07315 (2012). https://doi.org/10.1029/2012JA017832

Trondsen T, Unick C, Wyatt D, Kim J, Kim J, et al., Compact SWIR

imager for mapping temperature in the upper mesosphere/lower thermosphere, in AGU Fall Meeting 2021, New Orleans, LA, 13-17 Dec 2021.

Vallance Jones A, Gattinger RL, Quantitative spectroscopy of the aurora. IV. the spectrum of medium intensity aurora between 8800 Å and 11 400 Å, Can. J. Phys. 54, 2128-2133 (1976). https://doi.org/10.1139/p76-251

Wachter P, Schmidt C, Wüst S, Bittner M, Spatial gravity wave characteristics obtained from multiple OH(3–1) airglow temperature time series, J. Atmos. Sol. Terr. Phys. 135, 192-201 (2015). https://doi.org/10.1016/j.jastp.2015.11.008

Waldrop LS, Kerr RB, González SA, Sulzer MP, Noto J, et al., Generation of metastable helium and the 1083 nm emission in the upper thermosphere, J. Geophys. Res. 110, A08304 (2005). https://doi.org/10.1029/2004JA010855

Xu S, Vadas SL, Yue J, Thermospheric traveling atmospheric disturbances in austral winter from GOCE and CHAMP, J. Geophys. Res. Space Phys. 126, e2021JA029335 (2021). https://doi.org/10.1029/2021JA029335

Zhang Y, Paxton LJ, Morrison D, Wolven B, Kil H, et al., Nightside detached auroras due to precipitating protons/ions during intense magnetic storms, J. Geophys. Res. 110, A02206 (2005). https://doi.org/10.1029/2004JA010498

Zou Y, Nishimura Y, Lyons LR, Donovan EF, A statistical study of the relative locations of electron and proton auroral boundaries inferred from meridian scanning photometer observations, J. Geophys. Res. 117, A06206 (2012). https://doi.org/10.1029/2011JA017357